

Evidence for a grounding line fan at the onset of a basal channel under the ice shelf of Support Force Glacier (West Antarctica) revealed by reflection seismics.

Coen Hofstede¹, Sebastian Beyer¹, Hugh Corr³, Olaf Eisen^{1,2}, Tore Hattermann⁴, Veit Helm¹, Niklas Neckel¹, Emma C. Smith^{1,*}, Daniel Steinhage¹, Ole Zeising¹, and Angelika Humbert^{1,2}

¹Alfred Wegener Institute, Helmholtz Centre for Polar and Marine Research, Am Handelshafen 12, 27570, Bremerhaven, Germany

²University of Bremen, Klagenfurter Straße 28359, Bremen, Germany

³British Antarctic Survey, National Environmental Research Council, Cambridge, CB3 0ET, UK

⁴Norwegian Polar Institute, Framsenteret, Hjalmar Johansens gate 14, 9296 Tromsø, Norway

*Now at: School of Earth and Environment, University of Leeds, Leeds, LS2 9JT, UK

Correspondence: Coen Hofstede (coen.hofstede@awi.de)

Abstract. Curvilinear channels on the surface of an ice shelf indicate the presence of large channels at the base. Modeling studies have shown that where these surface expressions intersect the grounding line, they coincide with the likely outflow of subglacial water. An understanding of the initiation and the ice–ocean evolution of the basal channels is required to understand the present behavior and future dynamics of ice sheets and ice shelves. Here, we present focused active seismic and radar surveys of a basal channel, ~950 m wide and ~200 m high, and its upstream continuation beneath Support Force Glacier which feeds into the Filchner Ice Shelf, West Antarctica. Immediately seaward from the grounding line, below the basal channel, the seismic profiles show an 8 km long, 3.5 km wide and 200 m thick sediment sequence with chaotic reflections we interpret as a grounding line fan deposited by a subglacial drainage channel directly upstream of the basal channel. Further downstream the seabed has a different character, it consists of harder, stratified consolidated sediments, possibly bedrock, deposited under different glaciological circumstances. In contrast to the standard perception of a rapid change in ice shelf thickness just downstream of the grounding line, we find a very flat topography of the ice shelf base with an almost constant ice thickness gradient along-flow, indicating only little basal melting, but an initial widening of the basal channel, we ascribe to melting along its flanks. Our findings provide a detailed view of a more complex interaction between the ocean and subglacial hydrology to form basal channels in ice shelves.

1 Introduction

Ice shelf channels (Drews, 2015), also known as channels (Alley et al., 2016), surface channels (Marsh et al., 2016) or M-channels (Jeofry et al., 2018b) are narrow (a few km wide and 20–30 m deep mostly) long channels on the surfaces of ice shelves. They are often remotely detected with satellite imagery like MODIS (Moderate Resolution Imaging Spectroradiometer, 5 (Scambos et al., 2007)) or Landsat 8. These channels are a surface expression of a sub-ice shelf channel (Le Brocq et al., 2013), also known as basal channel (Marsh et al., 2016; Alley et al., 2016, 2019) or U-channel (Jeofry et al., 2018b), most often aligned to the ice flow direction but occasionally migrating across the ice flow direction. They typically are a couple of hundred metres high and a few km wide (Jeofry et al., 2018b; Drews et al., 2017). As locations of thinner ice these channels can induce ice shelf fracturing (Dow et al., 2018). Thus ice shelf channels potentially influence ice shelf stability, which in turn provides stability 10 of the ice sheet through the buttressing effect (Thomas and MacAyeal, 1982; Fürst et al., 2016). Alley et al. (2016) categorized three types of basal channels: (1) ocean sourced channels that do not intersect with the grounding line, (2) subglacially sourced channels that intersect the grounding line and coincide with modeled subglacial water drainage and (3) grounding line sourced types that intersect the grounding line but do not coincide with subglacial drainage of grounded ice. In the following we will use the term surface channel and basal channel to make a clear separation.

15 In the grounding line area of the Antarctic Ice Sheet, the location of modeled channelized meltwater flow often coincides with basal channels (and its surface expression, the surface channel) in the grounding line area (Le Brocq et al., 2013). This suggests subglacial drainage contributes to the formation of basal channels. According to Jenkins (2011) subglacial meltwater entering the ocean cavity at the grounding line forms a plume entraining warmer ocean water and causes increased subglacial melt beneath the ice shelf which drives the further evolution of channel geometry. This hypothesis is often graphically supported 20 by an idealized and conventional geometry of the sheet–shelf transition at the grounding line area: the ice–water contact (the underside of the ice shelf) rises steeply beyond the grounding line, thus allowing fresh water influx to form uprising melt plumes and then leveling out more horizontally further downstream (Le Brocq et al., 2013; Drews et al., 2017).

Drews et al. (2017) linked the formation of a basal channel to a potential esker upstream of the grounding line, noting that the channel dimensions are an order of magnitude larger than eskers in deglaciated areas. However, Beaud et al. (2018) found 25 that eskers are more likely to form under land terminating glaciers. Jeofry et al. (2018b) concluded that the basal channels at Foundation Ice Stream were initially formed by hard rock landforms upstream of the grounding line. Bathymetric surveys at different locations showing hard bedded landforms of similar dimensions as the basal channels confirmed this as a possibility. Alley et al. (2019), however, argued that shear margins of ice streams develop surface troughs continuing downstream of the grounding line. Once afloat, these surface troughs lead to the formation of basal channels during adjustment to hydrostatic 30 equilibrium, thereby forming a basal channel. Thus a channelized warm water plume is likely to incise a basal channel forming observed polynyas at the ice shelf front. Both hard rock landforms and surface troughs at shear margins of ice streams seem to cause basal channels. Unfortunately, key observations are often missing, e. g. on the type of material and structure of the bed upstream of a basal channel.

From noble gas samples at six locations beneath the Filchner Ice Shelf, Huhn et al. (2018) estimated a total freshwater influx of $177 \pm 95 \text{Gt/a}$, entering the Filchner Ice Shelf. At one location, downstream of Support Force Glacier (SFG), the noble gas sample indicated crustal origin and thus part of the freshwater influx having a grounded subglacial origin. We also know that the west side of SFG, where a surface channel is present, coincides with modeled channelized subglacial drainage (Le Brocq et al., 2013; Humbert et al., 2018). Thus we have good reason to assume there is subglacial drainage channel present at SFG.

Most field observations of surface channels and basal channels come from satellite imagery, airborne or ground penetrating radar. Although airborne radar gives a good impression of the shape of the ice shelf at larger scales, its trace distance is large (10 m) and primarily registers nadir reflections. The narrow aperture thus provides only limited insight into the precise geometry of the channel, especially steep structures like the flanks of the basal channel. In addition radar signals typically do not penetrate below wet ice-bed contacts, making it hard to determine the nature of subglacial material: is water exclusively present on hard bedrock or does the substrate also consist of sediments?

To investigate the ice–bed, ice–ocean characteristics we deployed an active source, high-resolution seismic survey concentrated at an isolated surface and basal channel on the west side of the sheet–shelf transition of SFG (Fig. 1). The highly resolved seismic signal allows complex subglacial structures like basal channels to be reconstructed given the larger aperture of the system compared to airborne radar. It also informs us about subglacial and ocean floor properties, as the signal penetrates through water containing substrata and the sub-shelf ocean cavity. This seismic survey, collected in January 2017, is supported by airborne radar data of the sheet–shelf transition of SFG collected later that month. Key questions we want to answer are: What initializes the surface and basal channel? How does it continue upstream of the grounding line? Is there any active subglacial drainage connected to the channel?

We first discuss the survey site and the different data sets, then the results of the seismic data analysis. Finally, we discuss the possible interpretations of our findings.

2 Survey area and data

2.1 Site description

SFG is an ice stream in Antarctica feeding into the Filchner Ice Shelf. The ice stream lies between Foundation Ice Stream in the southwest (also grid southwest) and Recovery Glacier in the northwest. The northward ice flow is constrained between the Dufek Massif (the northern part of the Pensacola Mountains) on the western side and the Argentina Range on the eastern side constraining the ice shelf for 50 km (Fig. 1). The drainage basin of SFG is poorly defined (Rignot et al., 2011). Although it drains from interior East Antarctica, it is linked to West Antarctica through the Filchner-Ronne Ice Shelf (Bingham et al., 2007). At the grounding line (GL) the ice is grounded 1200–1400 m below sea level (mbsl, WGS84 ellipsoid) with a surface velocity of 200 m/a. Upstream of the GL the bed is retrograde, it dips gently (slope of 0.28°) for some 20 km followed by a 400 m rise over the next 10 km and a fairly constant depth over the next 30 km (Fretwell et al., 2013). The survey target was a single and only surface channel (at the surface of the ice shelf) and its basal channel (at the base of the ice shelf) on the western

side of SFG, not influenced by other basal channels which might affect the ice dynamics or ice–seawater interaction. At the GL we performed a high-resolution seismic reflection survey consisting of two along-flow and three across-flow profiles (Fig. 1).

2.2 Ice surface velocities and grounding line position

Ice surface velocities were combined from Landsat-8 and TerraSAR-X derived velocity fields. Landsat-8 velocity fields were downloaded from the Global Land Ice Velocity Extraction from Landsat 8 (GoLIVE) database (Scambos et al., 2016). Here preference was given to 64 day repeat passes as a trade-off between accuracy and decorrelation (Fahnestock et al., 2016). Due to orbital constraints Landsat velocity estimates reach a maximum latitude of $\sim 82.7^\circ\text{S}$ which is just upstream of the grounding line of SFG (Figure 1a). In order to extend the velocities further south, we employed additional data takes from TerraSAR-X acquired in left looking mode. TerraSAR-X surface velocity fields were calculated by means of intensity offset tracking on single look complex imagery (e.g. Strozzi et al., 2002). Subsequently all velocity fields were filtered by the three step filtering procedure introduced by Lütting et al. (2017) and merged into a continuous velocity mosaic. Employing the same TerraSAR-X data as in the calculation of the velocity fields we were able to generate several coherent double differential interferograms which were used to slightly modify grounding line locations (Fig. 1c) obtained from the Deutsches Zentrum für Luft- und Raumfahrt (DLR) following well established methods (e.g. Rignot et al., 2011).

15 2.3 Airborne radar data

Late January 2017, the British Antarctic Survey (BAS) collected airborne ice-penetrating radar data with the PASIN2 system (an upgraded version of that described by Jeofry et al. (2018a)). The radar acquired data with a repetition frequency of 312.5 Hz, which was then stacked and processed with an unfocused SAR algorithm before being decimated to an equivalent along-track spacing of ~ 11 m. The onset of the basal reflection was then obtained with a semi-automated process and merged with a laser surface terrain mapper to give the ice thickness and bed elevation: a wave speed in ice of $0.168 \text{ m } \mu\text{s}^{-1}$ along with a 10 m firn correction was used.

2.4 Routing of subglacial water

To determine the subglacial water pathways we used a simple flux routing scheme to compute subglacial water pathways as described in Humbert et al. (2018). Subglacial water flow is governed by the hydraulic potential Φ (Shreve, 1972), which can be written as

$$\Phi = \rho_w g h_b + \rho_i g H, \quad (1)$$

where ρ_w is the density of water, g acceleration due to gravity, h_b bed elevation, ρ_i density of ice and H the ice thickness.

For the bed elevation h_b we used a combination of BEDMAP2 (Fretwell et al., 2013) and the airborne radar data. The airborne radar profiles were nested into the BEDMAP2 dataset using the continuous curvature splines in tension algorithm implemented in the Generic Mapping Tools (GMT, Smith and Wessel, 1990). Next to our airborne radar data we incorporated all regionally available Operation IceBridge MCoRDS L2 ice thickness measurements collected in 2009 and 2014 in our

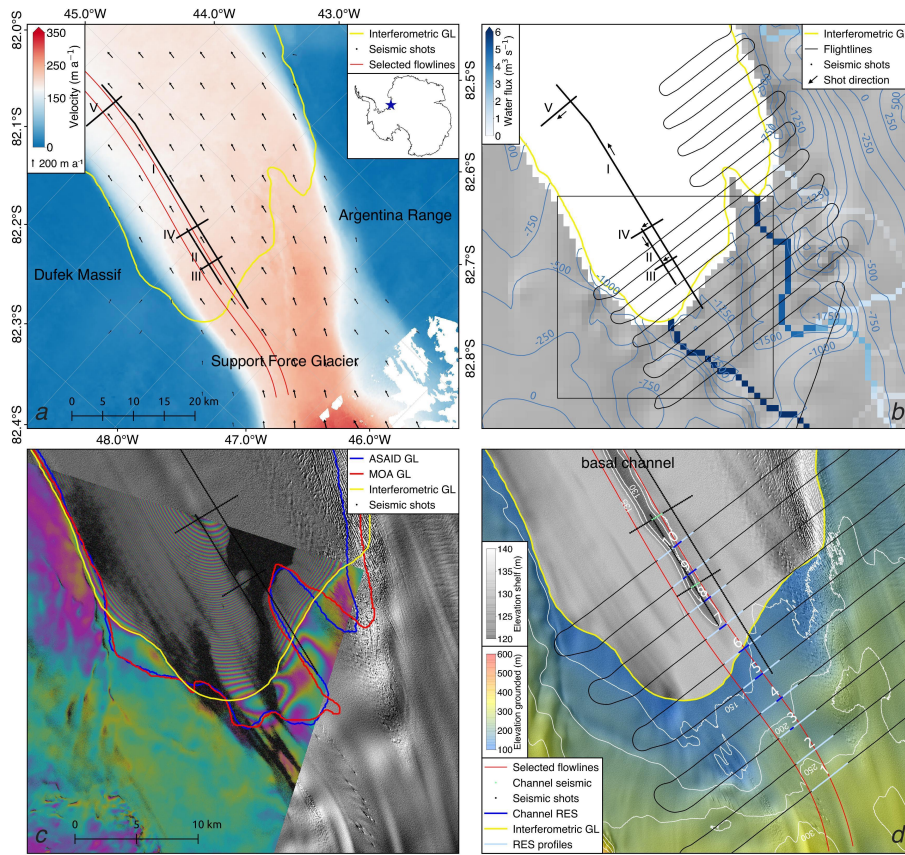


Figure 1. Location of the seismic and airborne radar surveys of the GL area of SFG. (a) Ice surface velocity map of the survey area. The seismic profiles are marked by black dots, along-flow profiles I and II and across-flow profiles III, IV and V. Two flow lines are marked in red and the GL in yellow. Inset: location of SFG in Antarctica. (b) Modeled subglacial water routing flux at SFG from the static hydrological potential. Shown are our updated bedrock compilation, a combination of BEDMAP2 and the collected airborne radar survey (thin black looping line). The shooting direction of the seismic profiles are shown by the arrows. The black rectangle marks the subregions of (b) and (c). (c) Three proposed GLs are marked in blue (ASAID Bindschadler et al. 2011), red (MODIS Scambos et al. 2007) and yellow (based on interferometry). The background is a shaded version of the 8 m Reference Elevation Model of Antarctica (REMA, Howat et al. 2019) overlaid by a TerraSAR-X interferogram used in the delineation of the grounding line. (d) The topography of the ice shelf (grey) indicates the surface channel. Numbered are loops 1 to 10 of the airborne radar data. Loops 1 to 5 are on the grounded part. Loops 7 to 10 represent the shelf, loop 6 is at the GL. In light blue we see the radar profiles shown in Figure 4. In green (seismic profiles) and dark blue (radar) we see the shot locations at the basal channel.

analysis (Paden et al., 2019). In order to achieve a smooth transition between BEDMAP2 and the radar data we further included data points from the gridded BEDMAP2 dataset within a 50 km buffer in the interpolation.

The modeled water routing (Fig. 1b) shows expected subglacial drainage routes entering the ocean cavity of SFG. Three influx entrances are predicted at SFG: A smaller one and larger one on the eastern side and one larger influx on the western

Table 1. Properties of the collected seismic profiles of SFG. Profile II is not listed here as it will not be discussed in the paper.

Profile	length (km)	Source	Direction
I	43.5	10 m (100 g) detonating cord	along-flow
III	4.2	150 g cartridge in borehole	across-flow
IV	6.0	10 m (100 g) detonating cord	across-flow
V	7.5	10 m (100 g) detonating cord	across-flow

side, close to the surface channel and the seismic survey area. Our seismic survey focussed on the larger influx entrance on the western side of SFG with a predicted water influx of $190 \times 10^3 \text{m}^3 \text{a}^{-1}$.

2.5 Seismic data recording

Early January 2017 we collected 71 km of seismic data divided over five profiles, numbered I to V (Fig. 1a, b). We used a 300 m snow streamer with 96 gimbaled 30 Hz vertical compressional wave (p-wave) sensors, pulled behind a Nansen sledge carrying the recording equipment (four Geometrics GEODE units recording 24 channels each). The record length was set to 5 s and the sample interval to 0.5 ms. We used a snowmobile to pull the sledge and streamer between shot locations. As a source we mostly used 10 m detonating cord of 10 g/m (so each shot used 100g PETN) placed 34 m in front of the near offset geophone and parallel to the snow streamer. At profile III we used 5 m deep drilled boreholes filled with 150 g pentolite cartridges. The shot spacing was half a streamer length, 150 m, resulting in single-fold data coverage. We refer to the single-fold data as profiles (Table 1). Profile II will not be discussed in the paper as it has a complex structure and hardly contributes to the paper.

During the data acquisition we collected 13 long offset gathers. At these shot locations we placed four shots of detonating cord at one location and recorded the shots at continuously decreasing offsets:

- Shot 1: offset 934 to 1234 m, streamer 934 m from the shot
- Shot 2: offset 634 to 934 m, streamer 634 m from the shot
- Shot 3: offset 334 to 634 m, streamer 334 m from the shot
- Shot 4: offset 34 to 334 m, streamer 34 m from the shot, profiling configuration

We used Shot 4 both in the long offset gather and for profiling. We created three types of processed data sets for the following applications:

- Profiles: Here the processing aim is to get an xz -image (x -axis: horizontal and z -axis: vertical) revealing the dimension and structure of the ice, ocean cavity and seabed. The data were band pass filtered (30–540 Hz), stacked, Kirchhoff time migrated and depth converted. Especially depth conversion of the time migrated profiles is important as the basal channel area has considerable topography over a relative flat seabed. As the seawater is a slow p-wave velocity layer, thickness

variation in the water column induces time delays in the underlying seabed and an apparent seabed topography in the time migrated profiles.

- Single shot gathers to determine the seismic reflection coefficient R : Here the aim is to map the amplitude values of different subsurface reflections and of the direct wave of raw shot gathers. Except for adding a geometry, these shots were not processed as any processing affects the amplitudes.
- Long-offset gathers: Here we combine four shots with sequentially increasing offset into one shot location with a long offset. The aim here is to register the Normal Move Out (NMO) of a reflection for long offsets (time delay of a reflection with increasing offset) from which subsurface seismic p-wave velocities can be derived. The data were processed such that the reflections are best visible. Processing steps include muting, spiking deconvolution, band pass and fk-filtering.

10 2.6 Seismic reflection and transmission coefficient at normal incidence

Reflectivity at a planar and specular two media interface in the subsurface depends on contrast of p-wave velocity (V_p), shear wave (s-wave) velocity (V_s), density (ρ) and the angle of incidence (θ) at the interface of the two considered media (Aki and Richards, 2002). At normal incidence the reflection coefficient R is solely determined by the contrast of the acoustic impedance ($Z = \rho V_p$) at the media interface:

$$R = \frac{Z_2 - Z_1}{Z_2 + Z_1} = \frac{\rho_2 V_{p2} - \rho_1 V_{p1}}{\rho_2 V_{p2} + \rho_1 V_{p1}}, \quad (2)$$

15 where subscripts 1 and 2 refer to upper and lower media. The θ -dependency of the reflection coefficient, $R(\theta)$, at a media interface can be expressed by:

$$R(\theta) = \frac{A_1(\theta)}{DA_0} r(\theta) e^{\alpha r(\theta)}, \quad (3)$$

with $A_1(\theta)$ being the amplitude of the primary reflection of the considered interface and A_0 being the source amplitude, D a directivity factor caused by the use of detonating cord as a source (when using point sources such as borehole shots $D = 1$), $r(\theta)$ the distance of the primary wave and α the seismic attenuation coefficient. These quantities can all be determined from 20 single shot records. The directivity factor D is discussed in subsection 2.8.

With a target depth of 1400 m or deeper, and an offset ranging from 33 to 330 m ($0.6^\circ \leq \theta \leq 6.7^\circ$), the reflections of the profiling shots are considered as being normal incidence. A shortcoming of using a relative small spread is that we are not able to plot the θ -dependency and perform an Amplitude-Versus-Angle (AVA) analysis of subglacial or seabed materials making identification less certain. Using the same values and lithology as Christianson et al. (2014) we calculated R at normal 25 incidence (Table 2) from the following media interfaces we encounter in our survey area:

- grounded ice–bed interface;
- shelf ice–seawater interface;
- seawater–seabed interface;

In all cases of considered media interfaces, the acoustic impedance of the upper medium, ice (grounded or shelf ice) or the sub-shelf seawater can be estimated quite accurately as the material (ice or seawater) is known and the acoustic impedance of the lower medium (subglacial material or seabed) is unknown. Using both equations we can determine the acoustic impedance of subglacial material and the seabed from single shots.

- 5 To calculate R at the seawater–seabed interface (R_{s-b} , where subscripts i, s and b refer respectively to *ice*, *seawater* and *bed* (both the bed upstream of the GL and seabed), respectively) we assume normal incidence. The smallest possible value for R is caused by an ice–seawater transition; with $Z_i = 3.44 \times 10^6 \text{ kg m}^{-2}\text{s}^{-1}$ and $Z_s = 1.45 \times 10^6 \text{ kg m}^{-2}\text{s}^{-1}$ we get:

$$R_{i-s} = \frac{Z_s - Z_i}{Z_s + Z_i} = \frac{(1.45 - 3.44) \times 10^6}{(1.45 + 3.44) \times 10^6} = -0.41. \quad (4)$$

The transmission coefficient T is given by:

$$T = \frac{2Z_1}{Z_2 + Z_1} = \frac{2\rho_1 V_{p1}}{\rho_2 V_{p2} + \rho_1 V_{p1}}. \quad (5)$$

- To calculate R_{s-b} we must take into account the energy loss at the ice shelf–seawater interface. To compensate for this energy loss we assume normal incidence and an abrupt transition at the ice–seawater interface. Under these assumptions and with the ice–seawater transmission coefficient ($T_{i-s} = 1.41$) and seawater–ice transmission coefficient ($T_{s-i} = 0.59$) we get

$$R_{s-b} = \frac{A_1(\theta)}{T_{i-s}T_{s-i}A_0} r(\theta)e^{\alpha r(\theta)} = \frac{A_1(\theta)}{0.83A_0} r(\theta)e^{\alpha r(\theta)}, \quad (6)$$

with $A_1(\theta)$ being the amplitude of the seabed reflection.

2.7 Seismic attenuation of the ice and seawater

- To determine the seismic attenuation α we need an estimate of the temperature of the shelf ice. We used temperature data from the 862 m long borehole FSW2 at the Filchner Ice Shelf at -44.22546°W , -80.56532°S , about 190 km downstream (northwest) of our survey area and another 275 km upstream from the calving front of the Filchner Ice Shelf. The installed thermistor chain showed an ice temperature range between -29°C at 10 m depth to -24°C at 650 m depth then increasing to -2.3°C at the base. As the ice shelf at the survey area is thicker (1300 m), we extrapolated the temperature curve. Using this temperature profile, a center frequency of 100 Hz, $V_p = 3750 \text{ m s}^{-1}$ we calculated average seismic attenuation of 0.2 km^{-1} for the entire ice column (Peters et al., 2012; Bentley and Kohnen, 1976).

We used the seawater temperature from the same borehole data, -2.3°C , to calculate the seismic attenuation of the water column. Assuming a constant temperature for the entire subglacial seawater column, we get an attenuation of 0.001 dB km^{-1} (Ainslie and McColm, 1998). This converts to $1.15 \times 10^{-4} \text{ km}^{-1}$ which is so low that we can ignore this component.

- With α of the ice and sea column known and Equations 6 and 3 we can calculate R . In general, one can say that the higher the water content of the lower medium Z_2 , the smaller is R (Table 2). If ice is the upper medium, the range of R is larger than if the seawater is the upper medium, making the interpretation of the seabed more sensitive to uncertainties. In general, R has the same trend i.e. the higher the water content of the seabed sediment, the smaller is R , but a distinction between subglacial unconsolidated or dilated till is not possible.

Table 2. Ranges of R for different media contrasts at normal incidence. Top: If the upper medium Z_1 is ice. Bottom: If the upper medium Z_1 is seawater. The acoustic impedances and lithologies of the lower media Z_2 are similar to Christianson et al. (2014).

Media contrasts with ice:	R min.	R max.
Lithified sediments/bedrock	0.30	0.67
Consolidated sediments	-0.05	0.18
Unconsolidated sediments	-0.08	0.03
Dilatant till	-0.11	0.00
Seawater	-0.42	-0.39
Media contrasts with seawater:	R min.	R max.
Lithified sediments/bedrock	0.62	0.67
Consolidated sediments	0.35	0.55
Unconsolidated sediments	0.28	0.41
Dilatant till	0.25	0.38

2.8 Determination of the source amplitude A_0

To determine A_0 we used the direct path method (Holland and Anandakrishnan, 2009), whereby the amplitudes of primary reflections of geophone pairs with a travel path ratio of 2 are compared. It was not possible to employ the alternative multiple bounce method (Smith, 1997), as the primary multiple is hardly visible in the data. Assuming α does not change over the travel path, A_0 can be calculated. As our geophones are vertically orientated and the direct wave is a diving wave (a continuously refracted wave due to the continuous densification of the firm pack (Schlegel et al., 2019)), we used pairs of traces at larger offsets (97 m and larger) from the source which causes the ray-path of the diving wave to arrive at angles closer to normal incidence.

The detonating cord, placed in front of and parallel to the streamer, makes the source directional. Detonation creates a wave front spreading cylindrically, perpendicular to the detonating cord orientation and semi-spherical at the ends of the cord. The cylindrically spreading wave front contains more energy and mostly agitates the subsurface whereas the spherically spreading wave front passes the streamer as a diving wave. This means we underestimate the source amplitude A_0 when using the direct path method.

At the ice-seawater interface, where the transition was abrupt, we determined A_0 by setting $R_{i-s} = -0.41$. At these transitions we know the acoustic impedance of the upper and lower media, namely ice and seawater, so here we can calibrate R_{i-s} . We refer to these shots as calibrated shots. Transitions from shelf ice to the seawater are not always acoustically abrupt, accreted ice or placelet ice may have formed at the base of the ice, giving (most often) larger values for R_{i-s} and $T_{i-s}T_{s-i}$. We considered 26 shots (21 at profile I, one at profile III, two at profile IV and two at profile V) of which eight (six at profile I, one at profile IV and one at profile V) had an abrupt ice-seawater transition at the ~ 9 m scale of vertical resolution. From these eight shots we derived the source amplitude A_0 reliably by setting $R_{i-s} = -0.41$ and compared this with A_0 derived from the

direct path method. The direct path method underestimates A_0 by a factor of 2.6, equivalent to the directivity factor D ($2.1 < D < 3.1$) from the cylindrically-spreading source. To compensate for the directivity of the source amplitude, we use DA_0 as the directionally compensated source amplitude as shown in Equation 3. The directionally compensated source amplitude has thus 19% uncertainty.

5 Using DA_0 at five shots resulted in $R_{i-s} < -0.41$. As we assumed $R_{i-s} = -0.41$ is the smallest possible value for R , we set $R_{i-s} = -0.41$ at these shots and also refer to these as calibrated shots. With these additional calibrated shots we have a total of 13 calibrated shots (10 at profile I, two at profile IV and one at profile V) of the considered 26 shots.

Based on the noise level preceding the primary reflection of the bed or seabed, we determined A_1 with 7% uncertainty. This means we determined R_{s-b} of the calibrated shots with 7% uncertainty. Of the remaining 13 uncalibrated shots, where
10 the directionally compensated source amplitude DA_0 has 19% uncertainty, R_{i-b} and R_{s-b} could be determined with 32% uncertainty.

3 Results and seismic interpretation

3.1 Seabed depth conversion

In the following we will present time migrated and depth converted profiles. Time migrated sections are not suitable to unravel
15 the subglacial structure of the seabed when the ice shelf thickness shows significant variability over short distances. This is the case around the basal channel where the base of the ice shelf has significant topography and the seabed is fairly flat. As the seawater is a low velocity layer ($V_p = 1425$ m/s) in comparison to ice ($V_p = 3750$ m/s), the thickness variation of the ice shelf causes significant time variation in the seabed returns. The time migrated profiles show an apparent topography (an almost mirrored version of the topography of the base of the ice shelf) in the seabed caused by the different time delays of the ice shelf
20 thickness. To derive the correct subsurface structure it is thus important to convert the migrated seismic profiles to depth. In general this works quite well but especially below the steep flanks of the basal channel the seawater–seabed morphology can not be properly recovered. The apparent morphology of the seabed is thus influenced by the topography of the ice shelf.

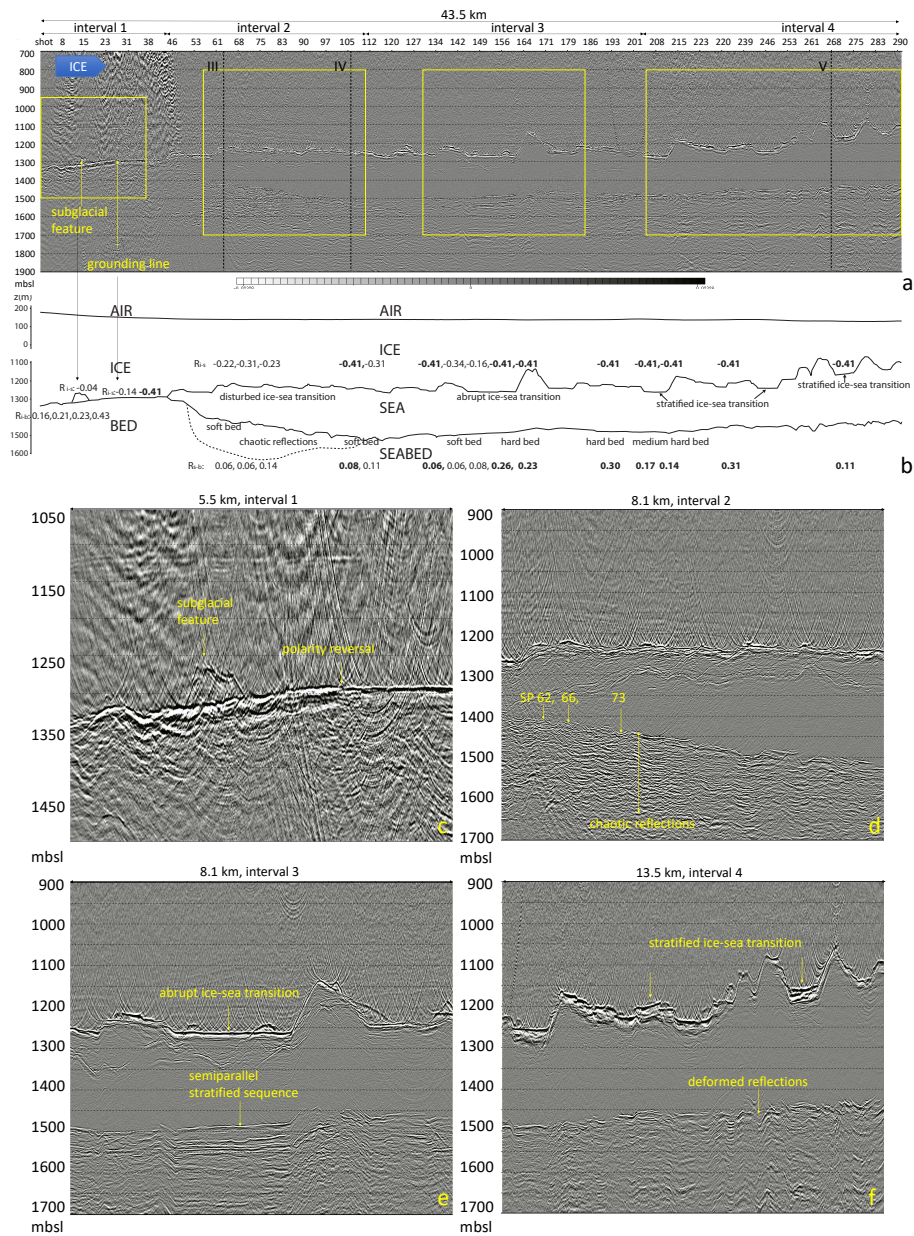


Figure 2. Profile I, its schematic diagram, and four zooms showing the discussed characteristics. (a) Time migrated and depth converted seismic profile I. The ice flow is from left to right. Shot point (SP) numbering is along the x -axis, increasing in shooting direction. The profile is divided into four intervals marked by the double headed arrows above the profile. The yellow frames represent the four zooms shown at figures (c) to (f). The crossings of profiles III, IV and V are marked by the black dashed lines. (b) A schematic diagram of profile I marking the boundaries of the ice surface, base and the seabed. The calculated reflection coefficients R are shown at their position. The bold numbers represent calibrated shots and the normal numbers uncalibrated shots. (c) Zoom of interval 1 showing the polarity reversal of the base at SP 26 and the subglacial feature at the flat bed. (d) The ~ 200 m thick sequence with chaotic reflections and little signal loss of the seabed marked by the dashed line in b. The seabed has reversed polarities at SP 62, 66 and 73. The transition to the harder semiparallel stratified material is transitional. (e) The ice-sea transition is abrupt and the seabed consists of harder, semi-parallel stratified sequence with fewer high amplitude reflections. (f) Here the ice-sea transition is stratified. The deformed reflections (apparent morphology) of the seabed are influenced by the concave cavities at the ice shelf base.

3.2 Seismic profile I

The first 3.9 km of the 43.5 km long profile I (Fig. 2a) are grounded ice. The GL is at shot point (SP) 26 where the polarity of the ice base reflection reverses. There are ten locations where $R_{i-s} = -0.41$ and the shots are calibrated (Fig. 2b), six where the ice-seawater transition was abrupt and we calibrated $R_{i-s} = -0.41$ and four locations, SP 208, 209, 231 and 273, where $R_{i-s} < -0.41$ and was set $R_{i-s} = -0.41$. Based on the topography, structure and the reflectivity of the ice-base contact and seabed contact, we distinguish four intervals in profile I.

Interval 1 is from SP 1 to SP 44 (Fig. 2 a and c). We see a flat bed in direct or close contact with overlying ice. The bed starts at 1350 mbsl at SP 1, rising to 1300 mbsl at SP 26 after which the bed stays at 1300 mbsl to SP 44. The polarity of the ice-bed contact of the grounded ice, we refer to in this paper as positive, reverses (becomes negative) after SP 26 and stays like that for the rest of the profile. The location of the polarity change is within 150 m of the GL derived by interferometry (Fig. 1c). From SP 4 to SP 22 R_{i-b} increases from 0.16 to 0.43. From SP 26 to SP 44, R_{i-s} is negative and decreases from -0.14 at SP 30 to -0.41 at SP 33. The ice is floating but the thickness of the seawater column is too small to be made out.

At the base of the grounded ice, between SP 11 and SP 17, there is an elongated feature that appears to lie on a harder flat bed. It is approximately 50 m high and 1200 m long and $R = -0.04$ at the ice bed contact. Our subsequent analysis shows this feature likely has evidence of a subglacial drainage channel and hereafter will be referred to as the subglacial feature.

Interval 2 is from SP 44 to SP 110 (Fig. 2 a and d). The ice-seawater contact, the base of the ice shelf, lies between 1220 to 1300 mbsl, has minor topography with concave cavities 20 to 50 m above the surrounding base, and has R_{i-s} values varying between $-0.41 \leq R_{i-s} \leq -0.22$. The ice-seawater contact is not abrupt, as the transition appears as an approximately 20 m sequence with chaotic reflections. This gradual ice-seawater transition probably leads to an increased energy loss and subsequently a larger (so less negative) R . At SP 44 the ocean cavity thickens as the seabed starts descending steeply to 1400 mbsl at SP 55 and then dips more gently to 1500 mbsl at SP 110. The polarity of the seabed contact is initially small and positive but occasionally, at SP 62, 66 and 73, negative. Between SP 55 and SP 107 the seabed consists of a ~ 8 km long and ~ 200 m thick sequence with chaotic reflections and little signal loss with increasing depth (hereafter referred to as the sequence with chaotic reflections). R_{s-b} varies between $0.06 \leq R_{s-b} \leq 0.14$. Downstream of SP 107 the character of the seabed gradually changes to a stratified sequence having less semiparallel, high amplitude, reflections.

Interval 3 lies between SP 110 and 204 (Fig. 2 a and e). The ice-seawater contact lies mostly between 1230 and 1260 mbsl, is (semi)horizontally terraced interchanged with concave cavities 50 to 150 m above the surrounding base, reaching 1140 mbsl at SP 164. The ice-seawater contact is more abrupt, especially in the lower (semi) horizontal terraces (SP 145 to SP 160 and SP 171 to SP 180). The seabed consists of a stratified sequence having less semiparallel, high amplitude, reflections, hereafter referred to as the stratified sequence with semiparallel reflections, and an increasing acoustic hardness downstream from $R = 0.06$ at SP 130 to $R = 0.3$ at SP 191. This harder, stratified sequence with semiparallel, reflections can best be observed between SP 145 and SP 160.

Interval 4 lies downstream of SP 204 (Fig. 2 a and f). The seawater-ice contact now rises from 1270 to 1100 m, is less terraced and has more concave cavities. The ice-seawater transition at the terraces is no longer abrupt but a 20 to 30 m

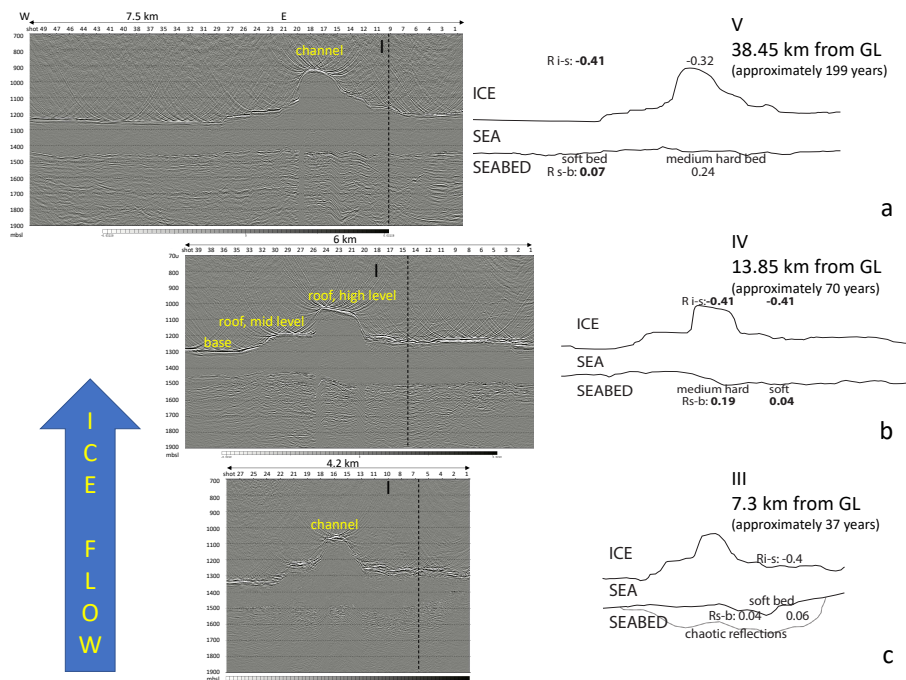


Figure 3. Profiles III, IV and V, and their schematic diagram, showing the development of the basal channel. The calculated reflection coefficients (bold represents calibrated shots) are shown at their position in the diagram. The ice flow sequence is from bottom to top. The crossing of the profile I is marked by the black dashed lines. The distance from the GL and the time lap for the ice to reach this distance is mentioned on the right side. The three profiles have been aligned across-flow with respect to the most westerly flow line of Figure 1a. (a) The most downstream profile V, with the high-level roof of the channel marked. (b) Profile IV, for clarity the high and mid-level roof of the channel as well as the base are marked. (c) The most upstream profile III. The sequence with chaotic reflections is marked in the schematic diagram by the dashed line.

stratified sequence of semiparallel reflections. This is especially visible in the lower terraces (SP 204 to SP 212, SP 243 to SP 250 and SP 269 to SP 276). At this interval the ice–seawater transition has been set to $R = -0.41$ (SP 273) because the calculated $R < -0.41$. At the seabed ($0.11 \leq R \leq 0.31$) is quite variable, larger than the second interval (SP 44–110) but not consistently high as in the third interval (SP 110–204). Despite the seabed being migrated and depth converted it (SP 250–291) shows apparent morphology: the deformed reflections are influenced by the concave cavities of the ice–seawater transition.

3.3 Seismic profiles III, IV and V

At profile III (Fig. 3) we used charges in 5 m deep boreholes whereas profiles IV and V were recorded with detonating cord. The borehole charges produce a ghost with 5 – 7 ms delay, not present when using detonating cord at the surface. This causes the source wavelet of the borehole charges is longer as with detonating cord charges. As a result, the ice–seawater and seawater–seabed contacts of profile III are not as well resolved (they appear more stratified) as for profiles IV and V.

The basal channel on all three profiles is terraced, especially on the western side where the channel has a mid- and a high-level roof, (Fig. 3b). On profiles III and IV, the lower level of the ice shelf base lies at 1330 mbsl and the roof of the basal channel, at 1050 mbsl. At profile V the character of the channel roof is more rounded but the terraces can still be made out. The base lies at 1250 mbsl and the high-level roof of the basal channel at 920 mbsl.

5 The seabed at the profiles lies between 1450 mbsl and 1500 mbsl (Fig. 3), but the migration and depth conversion (and thus the morphology) of the seabed under the steeper flanks of the basal channel, is not correct. Especially across-profiles IV and V have a flat seabed that only shows some apparent morphology under the steeper flanks of the basal channel.

Profile III crosses the ~ 200 m thick sequence with chaotic reflections of interval 2. The seabed shows this sequence is 3.5 km wide and present under the basal channel, extending and increasing somewhat in thickness east of the basal channel. The
10 sequence is absent on the eastern and western sides (start and end) of across-profile III. At SP 11 the sequence has $R_{s-b} = 0.04$ and we know that at the crossing (SP 7) with profile I the sequence has $R_{s-b} = 0.06$. At profiles IV and V the seabed below the basal channel has $R_{s-b} = 0.19$ and $R_{s-b} = 0.24$

3.4 Radar images of basal channel

We selected ten airborne radar profiles separated by 2.6 km in along-flow direction (Fig. 4) tracking the basal and, upstream of
15 the GL, the subglacial channel (the feature between the ice and bed upstream of the basal channel, probably water filled). They are ~ 3.75 km long, and their numbering corresponds to Figure 1d. The radar profiles are rotated 5° counterclockwise with respect to the seismic across-flow profiles. Profile 10 is 10.9 km downstream of the GL, profile 6 is at the GL (partly grounded and partly on shelf), and profile 1 is 12.8 km upstream of the GL.

In Figure 5 we combine the basal reflection of the ice of the ten migrated radar and the three seismic profiles in a schematic
20 diagram to track the development of the subglacial channel and basal channel along its flow line. All 3.75 km long profiles have been lined up against the westernmost flow line of Fig. 1a. The resolution of the radar data is not as good as that of the seismic data, so the shape of the basal channel can not be reconstructed as well, nevertheless, we can track it. On the grounded ice we can track the subglacial channel at profiles 3, 4, 5 and 6 where it increases in size from hardly distinguishable from the surrounding bed to 280 m at profile 6 at the grounding line and continues as a basal channel under the ice shelf. The basal
25 channel meanders up to profile 9 after which the three remaining profiles 10, IV and V show a consistent migration westward. The height of the subglacial and basal channel is hard to determine accurately, partly because of the poorer resolution of the radar profiles but also because it is hard to determine what the base of the ice shelf exactly is so the heights should be seen as an indication rather than an exact measurement. In general the height of the basal channel is constant between profiles 7 and IV and then increases its height to 205 m.

30 To see the changing geometry of the basal channel, we restrict ourselves to the migrated, depth converted seismic profiles that reproduce the shape of the basal channel more accurately than the radar profiles (Fig. 6). From profile III to IV (Fig. 6a), the terraced multi leveled roof of the channel stays preserved but widens from some 780 m to 920 m, rather than that the ice shelf thickness changes. The flanks of the basal channel become steeper but the height does not change noticeably although there may be some lowering in the center of the basal channel. From profile IV to V (Fig. 6b), the terraced basal channel

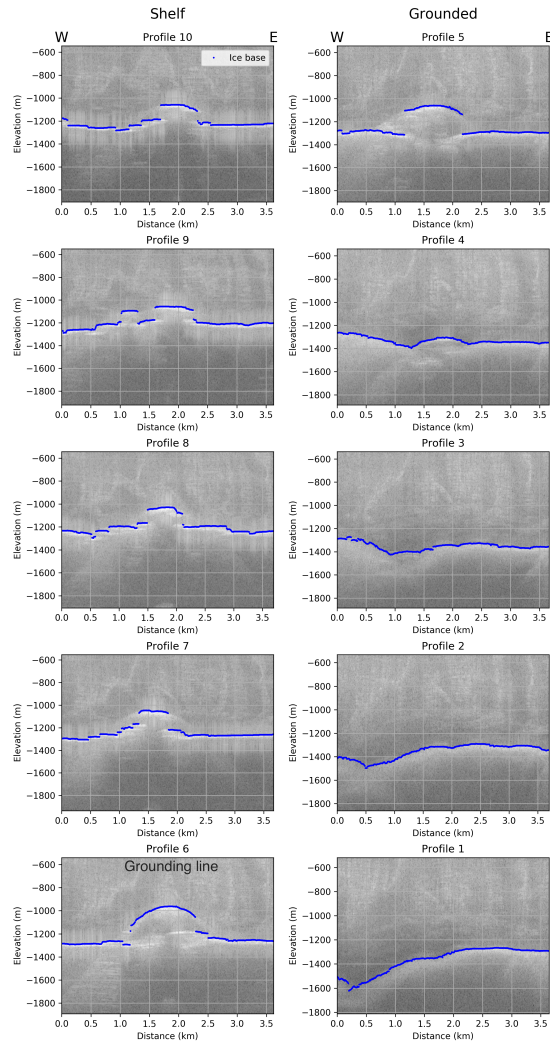


Figure 4. Return power, grey-scaled and depth converted radar profiles 1 to 10. Figure 1d shows their position. The ice flow direction is from bottom to top, starting with profile 1 (upstream) at the lower right corner up to 10 (downstream) in the upper left corner. The semi-automatically picked basal reflection (seawater and bed) of the ice is marked in blue. At profiles 1 to 5 the ice is grounded, profile 6 is at the grounding line and at profiles 7 to 10 the ice is floating.

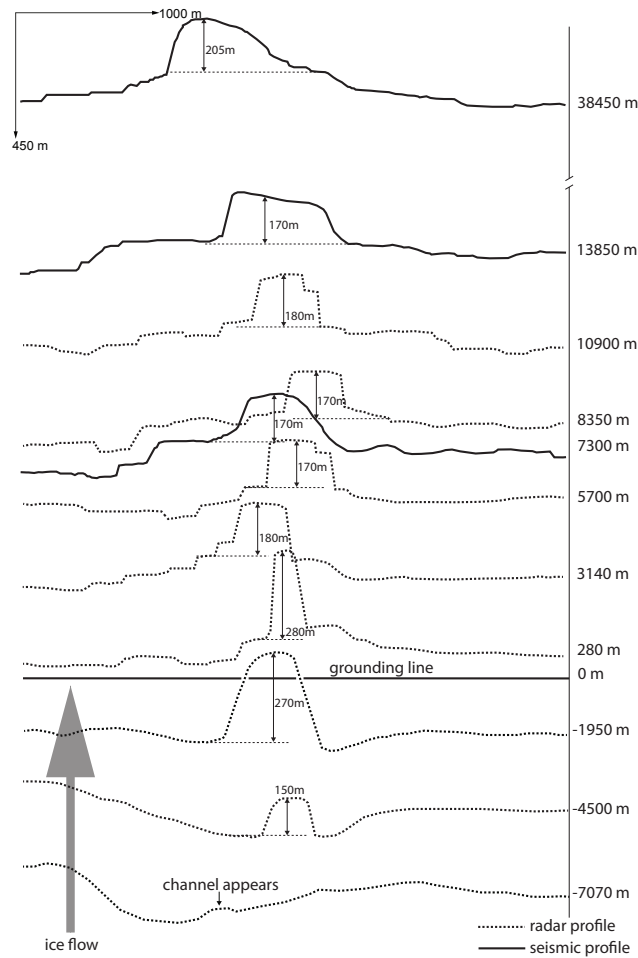


Figure 5. A schematic diagram of the shape and development of the subglacial channel under the grounded ice and basal channel under the ice shelf. The scheme combines the migrated radar (dashed) and seismic (continuous) profiles. The vertical axis shows the distances to the grounding line measured along the westerly flow line of Figure 1d.

becomes less pronounced and the base is shallower (i.e. the ice shelf is thinner). As a result profile V moved upward. The basal channel also moved westward with respect to profile IV so in a downstream direction. The flat roof of the channel becomes more rounded and the lower level roof on the western side, less pronounced.

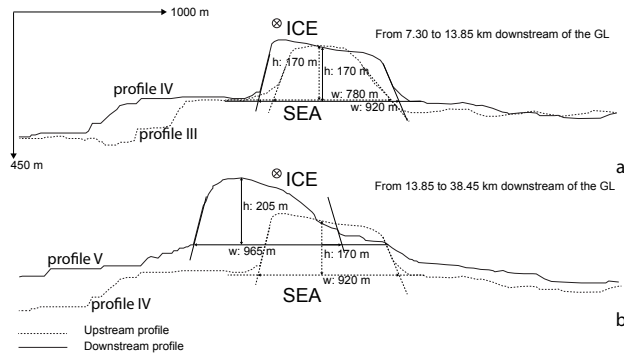


Figure 6. A schematic diagram of the ice shelf development around the basal channel derived from the three seismic across-flow profiles in Figure 3. Vertically, they are positioned with respect to the ice shelf surface so that the ice thickness can be compared. (a) Comparing profile III (dashed line) with IV (continuous line). (b) Comparing profile IV (dashed line) with V (continuous line).

4 Discussion

4.1 The grounding line position

At profile I the polarity of the basal reflection reverses from positive to permanently negative in downstream direction at SP 26 (Fig. 2a). As negative polarity indicates the presence of water at the base, this suggests the ice uncouples from the bed.

- 5 Between SP 30 and 33 we see a decrease in R from $R_{i-s} = -0.14$ to $R_{i-s} = -0.41$ which is probably caused by an increase in water content in the subglacial bed. At SP 33 the ice is in contact with the seawater. We recorded SP 26 at 17:06 UTC, January 1, 2017. According to five GPS stations 13 km downstream from the GL, this is 3.5 hrs after high tide at which time there was 1.5 m additional uplift on a tidal range of 2.6 m. As SP 26 lies within 150 m of the GL derived from interferometry we refer to the GL as the one provided by interferometry in the remainder of the paper.

10 4.2 The structure of the ice shelf and ocean cavity

- Looking at the structure of the ice sheet at the GL area of profile I (Fig. 2), we see an almost constant ice thickness gradient when the ice, initially flowing over a flat bed, passes the GL. Unlike the classic picture of the sheet–shelf transition, where rapid ice shelf thinning close to the GL causes a steeply rising ice shelf base, the sheet–shelf transition of SFG seems to be a mirrored version of this: SFG has a steeply descending seabed at SP 44 and an almost constant ice thickness downstream of the GL. This steeply descending seabed, the onset of the ocean cavity, probably determines the GL position. The absence of an ocean cavity at the flat ice shelf base upstream of SP 44 confirms this.

Generally we would expect the highest melt rates at the deepest part of the ice shelf, the GL, as that is where the melting point is lowest due to the pressure effect of the ocean. The topographically constrained ice flow, confirmed by the parallel flow lines (Fig. 1a) and the flat ice shelf base, allow us to use the ice thickness gradient as a first order approximation for basal melt

(Fig. 2). As the base of the ice shelf is initially flat, any topography in the base is likely to be caused by basal melt. The constant ice thickness gradient of the ice passing the GL suggests there is little basal melting at the GL of SFG.

Once in contact with the ocean cavity at SP 44, there is some basal melting as the base of the ice shelf has some topography but this increases in downstream direction as we see an increase in the number of and the magnitude of concave cavities in the ice base. Interval 2 has some topography but small compared to interval 3 and 4. Interval 3 has one pronounced concave cavity at SP 164 interchanged with lower terraces and interval 4 has several pronounced concave cavities, at SP 215 and downstream of SP 250, interchanged with lower terraces. Dutrieux et al. (2014) observed a similar ice shelf geometry and attributed the terrace shaped structure to a steplike thermohaline ocean structure causing organized melting.

That there is little melting at the GL increasing in downstream direction is also confirmed by the seismic profiles of Figure 6b. The ice shelf base of profiles III and IV does not change much in depth but the basal channel itself widens. At Pine Island Glacier this channel widening was ascribed to ice dynamics, i.e. convergence at ice shelf surface and divergence at ice shelf base (Dutrieux et al., 2013; Vaughan et al., 2012). At SFG we observed no noticeable ice convergence at the surface channel, at least not distinguishable from the noise level. Between profiles IV and V we observe a general thinning of the ice shelf, both, above the basal channel and outside of it. Profile V crosses profile I in interval 4 where there is increased basal melting of the ice shelf.

4.3 Properties of the seabed

At profile I we recorded 10 calibrated and 11 uncalibrated shots. At the calibrated shots we will use R , having 7% uncertainty, for interpretation. At the uncalibrated shots where R has 32% uncertainty, we use the trend of the magnitude and polarity of R for interpretation rather than the actual value.

At all the places where the ice–seawater contrast is not abrupt, the propagating p-wave, traveling from the ice shelf into the seawater, encounters a series of transmissions and reflections rather than a single transmission. The total amplitude loss over such a stratified ice–seawater contrast is probably larger than our assumed transition of Equation 6. At these places we most likely underestimate R_{s-b} .

While still grounded, we see an increase in R_{i-b} from 0.16 to 0.41 over a 3.9 km distance. As we find it less likely that the subglacial material changes drastically over this short along-flow interval and the acoustic impedance Z of the ice is constant, we attribute this steady increase in acoustic impedance of the subglacial material potentially to increasing compaction, as has been observed by Christianson et al. (2013). We interpret the bed of the grounded ice thus as subglacial till.

Once the ice passed the GL at SP 26, the floating ice stays close to its flat base down to SP 44 when the seabed starts to descend steeply. The seabed downstream, of SP 44 consists of two distinguishable environments. At interval 2, close to the GL, we have an 8 km long, and 200 m thick sequence with chaotic reflections that changes into a stratified sequence with semiparallel, reflections at intervals 3 and 4. The sequence with chaotic reflections close to the GL, having smaller values for R_{s-b} , consists of softer, more porous material than the stratified sequence with semiparallel, reflections. The softness is confirmed by the occasionally negative polarity at the steeper downslope of the seabed. We interpret the sequence as an unconsolidated sedimentary sequence.

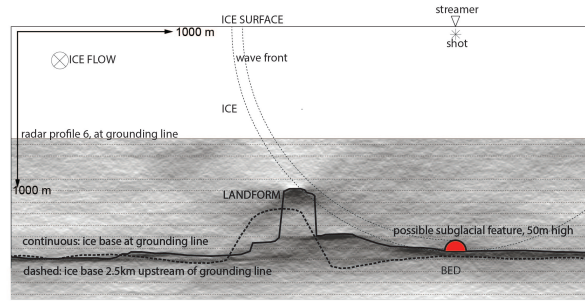


Figure 7. Cross section of the seismic recording geometry of profile I during SP 11 to 17 when the subglacial feature was recorded. The shooting and ice-flow direction are into the page, perpendicular to the cross section. The continuous and dashed black lines represent the ice base at the GL (continuous, profile 6), and 2 km upstream (dashed, profile 5) from the GL. The subglacial feature can either be at nadir in which case its dimensions are represented by the red semicircle or the feature can be off-nadir in which case the feature likely represents the top of the subglacial channel from profile 6. The spherical wave front (dashed quarter circle) shows the off-nadir reflections from the top the basal channel (profile 6) arrive just before the nadir flat bed reflections (so when no semicircle would be present).

The stratified sequence with semiparallel, reflections generally has higher values for R_{s-b} , indicating a harder material. This is particularly clear in interval 3, where $0.23 \leq R_{s-b} \leq 0.30$. The seabed structure representative for this second type of environment is most clearly visible between SP 146 and 161, where the flat featureless and abrupt ice–sea contact does not influence the seabed morphology. In interval 4 we calculated lower values for R_{s-b} but these low values all have a stratified ice–seawater contact above them and so the amplitude loss at the ice–sea transition may be larger than is accounted for and probably underestimates R_{s-b} . Based on $R_{s-b} \approx 0.31$, we interpret them as consolidated sediments but can not exclude bedrock. In any case, this part of the seabed has properties of an eroded surface, where softer deposits are missing. It could have been created during periods of higher ice-dynamic activity, e.g. during one or several advances of SFG during the last glacial into LGM positions of maximum advance.

10 4.4 Characteristics of the subglacial feature

At profile I, below the grounded ice between SP 11 and 17, we see the subglacial feature. If this seismic event is from nadir, it would be a separate, 1200 m long and approximately 50 m high, subglacial feature on a hard bed, its dimensions represented by the red semi-circle in Fig. 7. The reflection coefficient $R_{i-b} = -0.04$ represents an ice–unconsolidated, water saturated sediments contact so most likely the subglacial feature would be subglacial conduit on a hard flat bed. A 50 m high conduit would show up in the profiles 5 and 6 but both radar profiles 5 and 6 show a flat base at nadir. We also do not see any evidence of any other subglacial channel entering the ocean cavity on the western side of SFG.

A more likely interpretation is that the subglacial feature is from off-nadir and represents the top of the subglacial channel connecting to the basal channel Fig. 5. The spherically spreading wave front from the off nadir reflections of the subglacial

channel arrive before the nadir bed reflections (Fig. 7). When the subglacial channel reaches the dimension of profile 6 this is probably the case. We interpret the subglacial feature as the top of the ~280 m subglacial channel approaching the GL.

4.5 The subglacial hydrological interpretation

Our subglacial drainage model predicts a significant ($190 \times 10^3 \text{m}^3 \text{a}^{-1}$) freshwater influx on the western side of the ice shelf of SFG (Fig. 1b). At the grounded ice of SFG profiles 3, 4, 5 and 6 show a subglacial channel connecting to the basal channel at the grounding line. Over a length of 7 km approaching the GL the subglacial channel increases its size from hardly distinguishable from the bed to a 280 m height at the grounding line. The increase in size, when approaching the grounding line, is likely caused by the ocean interacting with the subglacial channel due to tidal motion, thereby melting the channel walls, as suggested by Drews et al. (2017), Horgan et al. (2013) and modeled by Walker et al. (2013). Once passed the grounding line this wide opening of the subglacial channel adjusts to hydrostatic equilibrium and forms the basal and surface channel in which the subglacial drainage water incises. This setting is similar to the subglacial estuary described by Horgan et al. (2013). Because the subglacial channel connects to the only basal channel at the western side of the ice shelf, and because we have a large subglacial drainage influx modeled at the western side of the ice shelf, we interpret the subglacial channel to be a subglacial drainage channel.

The grounded part of profile I consists of a sediment layer and, judging by its reflectivity, becoming more consolidated closer to the grounding line. So the drainage channel probably travels over a layer of subglacial sediments with varying consolidation. The exact nature of the subglacial drainage system we do not know but the radar and seismic profiles do suggest channelized flow close to the grounding line. Possibly we are dealing with a channel that, upstream and outside the survey area, is coupled to a surrounding distributed system as described by Hewitt (2011). Close to the grounding line channelized flow is favorable which corresponds to our observations.

Profile I (1.5 km east of the basal channel) shows an 8 km long and ~200 m thick sedimentary sequence with chaotic reflections just downstream of the GL. Profile III, crossing this sedimentary sequence with chaotic reflections, shows this sequence is 3.5 km wide and only present under the basal channel. Both on the far eastern and western side of profile III there is hardly any structure in the seabed except right under the channel. This sedimentation has most likely been transported by the subglacial drainage channel and consists of unconsolidated, probably subglacial terrestrial sediments. Based on profile I and III we interpret the sedimentation to be point sourced (the subglacial drainage channel) and fan shaped forming a grounding line fan (Powell, 1990) or an ice-proximal fan (Batchelor and Dowdeswell, 2015). This explains the chaotic reflections in this sedimentary sequence and this material being softer as the further downstream part of the sea bed.

What is unusual here is that the fan has formed under the ice shelf of SFG, a region without surface melt which is a characteristic of fans (Powell and Alley, 2013). But we do have evidence for channelized flow at the grounding line, a noble gas sample suggesting freshwater observation influx of terrestrial origin likely (Huhn et al., 2018) and a significant modeled channelized freshwater influx on the western side of SFG confirmed by the presence of a single basal channel on the western side. We also have an unusual ocean cavity with a steeply descending seabed and a stable grounding line. These are typical

conditions for the formation of a fan at the grounding line (Powell, 1990; Powell and Alley, 2013; Batchelor and Dowdeswell, 2015).

5 Conclusions

We investigated the characteristics of a subglacial channel continuing as a basal channel across the grounding line of the Support Force Glacier. As this is the only subglacial channel, basal channel system on the western side of Support Force Glacier subglacial drainage takes place through channelized flow close to the grounding line. Our observations concur with the categorization of Alley et al. (2019), i.e. subglacially sourced channels that intersect the grounding line and coincide with modeled subglacial water drainage. We find no evidence for the hypothesis the basal channel is initially formed by a landform as suggested by Jeofry et al. (2018b). The increase in channel height close to the grounding line is probably caused by the ocean interacting with the subglacial channel thereby increasing its height as suggested by Horgan et al. (2013) and Walker et al. (2013).

In seismic profiles I and III at the seabed, close to the grounding line, we identify an 8 km long, 3.5 km wide and 200 m thick, soft, sedimentary sequence with chaotic reflections that most likely have been deposited by the subglacial channel. This makes the 200 m sedimentary sequence point sourced and fan shaped and so we interpret this sequence as a grounding line fan which is unusual for ice shelves.

Further downstream the seabed consists of harder, stratified consolidated sediments with semiparallel reflections, possibly also bedrock. We attribute these two units to originate from different development phases: whereas the harder sequence is potentially a left-over from a farther advanced grounding line, e.g. coming along with stronger erosion during advances into the LGM, the softer sediment sequence seems to be the result of comparatively recent post-LGM and Holocene grounding line depositions.

Apart from the basal channel and individual concave cavities, the base of the ice shelf downstream of the grounding line is relatively flat, indicating that basal melt rates are relatively low. We attribute the observed widening of the basal channel to melting along its flanks, which we also observe at the flanks of concave cavities in the ice shelf base. The melting increases further in downstream direction. To date it is unlikely that warmer water is already in the cavity near the grounding line. But even if it were, the geometry of the steeply descending seabed downstream of the grounding line would limit the direct contact of potentially warmer water with the ice shelf base, thus limiting basal melt rates, unless the cavity was fully flooded with warmer water. This is in contrast to the typically envisaged geometry and ice–ocean interaction at grounding lines, which often envisage a steeply rising ice shelf base just downstream of grounding lines, where circulation is dominated by the ice pump mechanism. With our improved characterization of the grounding line area of SFG, future modeling studies should investigate how differently this region might react to the presence of warm deep water in the cavity than for instance the glaciers in the Amundsen Sea Embayment region and thus quantify the role of the seabed geometry.

Acknowledgements. The Filchner Ice Shelf Project (FISP) was funded by the AWI Strategy Fund. The Grounding Line Location (GLL) product was provided by DLR via ESA CCI Antarctic Ice Sheet. Hugh Corr was supported by the UK Natural Environment Research Council large grant "Ice shelves in a warming world: Filchner Ice Shelf System" (NE/L013770/1). Some data used in this study were acquired by NASA's Operation IceBridge. TerraSAR-X data used for grounding line detection and surface velocities were made available through DLR proposal HYD2059. Niklas Neckel received funding from the European Union's Horizon 2020 research and innovation program under grant agreement No 689443 via project iCUPE (Integrative and Comprehensive Understanding on Polar Environments). We thank the field guides Dave Routledge and Bradley Morrell for their unwavering guidance and support. We also thank BAS for their logistic support and hospitality. A special thanks goes to the pilots delivering the hardware at the right time at the right remote place. Without them, this survey would have been impossible.

References

- Ainslie, M. A. and McColm, J. G.: A simplified formula for viscous and chemical absorption in sea water, *The Journal of the Acoustical Society of America*, 103, 1671–1672, <https://doi.org/10.1121/1.421258>, <https://doi.org/10.1121/1.421258>, 1998.
- Aki, K. and Richards, P. G.: *Quantitative Seismology*, University Science Books, 2 edn., <http://www.amazon.com/exec/obidos/redirect?tag=citeulike07-20&path=ASIN/0935702962>, 2002.
- Alley, K. E., Scambos, T. A., Siegfried, M. R., and Fricker, H. A.: Impacts of warm water on Antarctic ice shelf stability through basal channel formation, *Nature Geoscience*, 9, 290 EP –, <https://doi.org/10.1038/ngeo2675>, 2016.
- Alley, K. E., Scambos, T. A., Alley, R. B., and Holschuh, N.: Troughs developed in ice-stream shear margins precondition ice shelves for ocean-driven breakup, *Science Advances*, 5, eaax2215, <https://doi.org/10.1126/sciadv.aax2215>, <http://advances.sciencemag.org/content/5/10/eaax2215.abstract>, 2019.
- Batchelor, C. and Dowdeswell, J.: Ice-sheet grounding-zone wedges (GZWs) on high-latitude continental margins, *Marine Geology*, 363, 65 – 92, <https://doi.org/https://doi.org/10.1016/j.margeo.2015.02.001>, <http://www.sciencedirect.com/science/article/pii/S0025322715000304>, 2015.
- Beaud, F., Flowers, G. E., and Venditti, J. G.: Modeling Sediment Transport in Ice-Walled Subglacial Channels and Its Implications for Esker Formation and Proglacial Sediment Yields, *Journal of Geophysical Research: Earth Surface*, 123, 3206–3227, <https://doi.org/10.1029/2018JF004779>, <https://agupubs.onlinelibrary.wiley.com/doi/abs/10.1029/2018JF004779>, 2018.
- Bentley, C. R. and Kohnen, H.: Seismic refraction measurements of internal friction in Antarctic ice, , 81, 1519–1526, 1976.
- Bindschadler, R., Choi, H., Wichlacz, A., Bingham, R., Bohlander, J., Brunt, K., Corr, H., Drews, R., Fricker, H., Hall, M., Hindmarsh, R., Kohler, J., Padman, L., Rack, W., Rotschky, G., Urbini, S., Vornberger, P., and Young, N.: Getting around Antarctica: new high-resolution mappings of the grounded and freely-floating boundaries of the Antarctic ice sheet created for the International Polar Year, *The Cryosphere*, 5, 569–588, <https://doi.org/10.5194/tc-5-569-2011>, <https://www.the-cryosphere.net/5/569/2011/>, 2011.
- Bingham, R. G., Siegert, M. J., Young, D. A., and Blankenship, D. D.: Organized flow from the South Pole to the Filchner-Ronne ice shelf: An assessment of balance velocities in interior East Antarctica using radio echo sounding data, *Journal of Geophysical Research: Earth Surface*, 112, <https://doi.org/10.1029/2006JF000556>, <https://agupubs.onlinelibrary.wiley.com/doi/abs/10.1029/2006JF000556>, 2007.
- Christianson, K., Parizek, B. R., Alley, R. B., Horgan, H. J., Jacobel, R. W., Anandakrishnan, S., Keisling, B. A., Craig, B. D., and Muto, A.: Ice sheet grounding zone stabilization due to till compaction, *Geophysical Research Letters*, 40, 5406–5411, <https://doi.org/10.1002/2013GL057447>, <https://agupubs.onlinelibrary.wiley.com/doi/abs/10.1002/2013GL057447>, 2013.
- Christianson, K., Peters, L. E., Alley, R. B., Anandakrishnan, S., Jacobel, R. W., Riverman, K. L., Muto, A., and Keisling, B. A.: Dilatant till facilitates ice-stream flow in northeast Greenland, *Earth and Planetary Science Letters*, 401, 57–69, <https://doi.org/10.1016/j.epsl.2014.05.060>, 2014.
- Dow, C. F., Lee, W. S., Greenbaum, J. S., Greene, C. A., Blankenship, D. D., Poinar, K., Forrest, A. L., Young, D. A., and Zappa, C. J.: Basal channels drive active surface hydrology and transverse ice shelf fracture, *Science Advances*, 4, <https://doi.org/10.1126/sciadv.aao7212>, <https://advances.sciencemag.org/content/4/6/eaao7212>, 2018.
- Drews, R.: Evolution of ice-shelf channels in Antarctic ice shelves, *The Cryosphere*, 9, 1169–1181, <https://doi.org/10.5194/tc-9-1169-2015>, <https://www.the-cryosphere.net/9/1169/2015/>, 2015.

- Drews, R., Pattyn, F., Hewitt, I. J., Ng, F. S. L., Berger, S., Matsuoka, K., Helm, V., Bergeot, N., Favier, L., and Neckel, N.: Actively evolving subglacial conduits and eskers initiate ice shelf channels at an Antarctic grounding line, *Nature Communications*, 8, 15228, <https://doi.org/10.1038/ncomms15228>, <https://doi.org/10.1038/ncomms15228>, 2017.
- 5 Dutrieux, P., Vaughan, D. G., Corr, H. F. J., Jenkins, A., Holland, P. R., Joughin, I., and Fleming, A. H.: Pine Island glacier ice shelf melt distributed at kilometre scales, *The Cryosphere*, 7, 1543–1555, <https://doi.org/10.5194/tc-7-1543-2013>, <https://www.the-cryosphere.net/7/1543/2013/>, 2013.
- Dutrieux, P., Stewart, C., Jenkins, A., Nicholls, K. W., Corr, H. F. J., Rignot, E., and Steffen, K.: Basal terraces on melting ice shelves, *Geophysical Research Letters*, 41, 5506–5513, <https://doi.org/10.1002/2014GL060618>, <https://agupubs.onlinelibrary.wiley.com/doi/abs/10.1002/2014GL060618>, 2014.
- 10 Fahnestock, M., Scambos, T., Moon, T., Gardner, A., Haran, T., and Klinger, M.: Rapid large-area mapping of ice flow using Landsat 8, *Remote Sensing of Environment*, 185, 84 – 94, <https://doi.org/10.1016/j.rse.2015.11.023>, <http://www.sciencedirect.com/science/article/pii/S003442571530211X>, *landsat 8 Science Results*, 2016.
- Fretwell, P., Pritchard, H. D., Vaughan, D. G., Bamber, J. L., Barrand, N. E., Bell, R., Bianchi, C., Bingham, R. G., Blankenship, D. D., Casassa, G., Catania, G., Callens, D., Conway, H., Cook, A. J., Corr, H. F. J., Damaske, D., Damm, V., Ferraccioli, F., Forsberg, R., Fujita, S., Gim, Y., Gogineni, P., Griggs, J. A., Hindmarsh, R. C. A., Holmlund, P., Holt, J. W., Jacobel, R. W., Jenkins, A., Jokat, W., Jordan, T., King, E. C., Kohler, J., Krabill, W., Riger-Kusk, M., Langley, K. A., Leitchenkov, G., Leuschen, C., Luyendyk, B. P., Matsuoka, K., Mouginit, J., Nitsche, F. O., Nogi, Y., Nost, O. A., Popov, S. V., Rignot, E., Rippin, D. M., Rivera, A., Roberts, J., Ross, N., Siegert, M. J., Smith, A. M., Steinhage, D., Studinger, M., Sun, B., Tinto, B. K., Welch, B. C., Wilson, D., Young, D. A., Xiangbin, C., and Zirizzotti, A.: Bedmap2: improved ice bed, surface and thickness datasets for Antarctica, *The Cryosphere*, 7, 375–393, <https://doi.org/10.5194/tc-7-375-2013>, <https://www.the-cryosphere.net/7/375/2013/>, 2013.
- 20 Fürst, J. J., Durand, G., Gillet-Chaulet, F., Tavard, L., Rankl, M., Braun, M., and Gagliardini, O.: The safety band of Antarctic ice shelves, *Nature Climate Change*, 6, 479–482, <https://doi.org/10.1038/nclimate2912>, <https://doi.org/10.1038/nclimate2912>, 2016.
- Hewitt, I. J.: Modelling distributed and channelized subglacial drainage: the spacing of channels, *Journal of Glaciology*, 57, 302–314, <https://doi.org/10.3189/002214311796405951>, 2011.
- 25 Holland, C. and Anandakrishnan, S.: Subglacial seismic reflection strategies when source amplitude and medium attenuation are poorly known, *J. Glaciol.*, 55, 931–937, 2009.
- Horgan, H., Alley, R., Christianson, K., Jacobel, R., Anandakrishnan, S., Muto, A., Beem, L., and Siegfried, M.: Estuaries beneath ice sheets, *Geology*, 41, *textit[in press]*, <https://doi.org/10.1130/G34654.1>, 2013.
- Howat, I. M., Porter, C., Smith, B. E., Noh, M.-J., and Morin, P.: The Reference Elevation Model of Antarctica, *The Cryosphere*, 13, 665–674, <https://doi.org/10.5194/tc-13-665-2019>, <https://www.the-cryosphere.net/13/665/2019/>, 2019.
- 30 Huhn, O., Hattermann, T., Davis, P. E. D., Dunker, E., Hellmer, H. H., Nicholls, K. W., Østerhus, S., Rhein, M., Schröder, M., and Sültenfuß, J.: Basal Melt and Freezing Rates From First Noble Gas Samples Beneath an Ice Shelf, *Geophysical Research Letters*, 45, 8455–8461, <https://doi.org/10.1029/2018GL079706>, <https://agupubs.onlinelibrary.wiley.com/doi/abs/10.1029/2018GL079706>, 2018.
- Humbert, A., Steinhage, D., Helm, V., Beyer, S., and Kleiner, T.: Missing Evidence of Widespread Subglacial Lakes at Recovery Glacier, Antarctica, *Journal of Geophysical Research: Earth Surface*, 123, 2802–2826, <https://doi.org/10.1029/2017JF004591>, <https://agupubs.onlinelibrary.wiley.com/doi/abs/10.1029/2017JF004591>, 2018.
- 35 Jenkins, A.: Convection-Driven Melting near the Grounding Lines of Ice Shelves and Tidewater Glaciers, *J. Phys. Oceanogr.*, 41, 2279 – 2294, 2011.

- Jeofry, H., Ross, N., Corr, H. F. J., Li, J., Morlighem, M., Gogineni, P., and Siegert, M. J.: A new bed elevation model for the Weddell Sea sector of the West Antarctic Ice Sheet, *Earth System Science Data*, 10, 711–725, <https://doi.org/10.5194/essd-10-711-2018>, <https://www.earth-syst-sci-data.net/10/711/2018/>, 2018a.
- Jeofry, H., Ross, N., Le Brocq, A., Graham, A. G. C., Li, J., Gogineni, P., Morlighem, M., Jordan, T., and Siegert, M. J.: Hard rock landforms generate 130 km ice shelf channels through water focusing in basal corrugations, *Nature Communications*, 9, 4576, <https://doi.org/10.1038/s41467-018-06679-z>, <https://doi.org/10.1038/s41467-018-06679-z>, 2018b.
- Le Brocq, A. M., Ross, N., Griggs, J. A., Bingham, R. G., Corr, H. F. J., Ferraccioli, F., Jenkins, A., Jordan, T. A., Payne, A. J., Rippin, D. M., and Siegert, M. J.: Evidence from ice shelves for channelized meltwater flow beneath the Antarctic Ice Sheet, *Nature Geoscience*, 6, 945 EP –, <https://doi.org/10.1038/ngeo1977>, 2013.
- 10 Lüttig, C., Neckel, N., and Humbert, A.: A Combined Approach for Filtering Ice Surface Velocity Fields Derived from Remote Sensing Methods, *Remote Sensing*, 9, <https://doi.org/10.3390/rs9101062>, <https://www.mdpi.com/2072-4292/9/10/1062>, 2017.
- Marsh, O. J., Fricker, H. A., Siegfried, M. R., Christianson, K., Nicholls, K. W., Corr, H. F. J., and Catania, G.: High basal melting forming a channel at the grounding line of Ross Ice Shelf, Antarctica, *Geophysical Research Letters*, 43, 250–255, <https://doi.org/10.1002/2015GL066612>, <https://agupubs.onlinelibrary.wiley.com/doi/abs/10.1002/2015GL066612>, 2016.
- 15 Paden, J., Li, J., Leuschen, C., Rodriguez-Morales, F., and Hale., R.: 2010, updated 2019. IceBridge MCoRDS L2 Ice Thickness, Version 1., Boulder, Colorado USA. NASA National Snow and Ice Data Center Distributed Active Archive Center., <https://doi.org/10.5067/GDQ0CUCVTE2Q>, 2019.
- Peters, L. E., Anandakrishnan, S., Alley, R. B., and Voigt, D. E.: Seismic attenuation in glacial ice: A proxy for englacial temperature, *J. Geophys. Res.*, 117, F02008, <https://doi.org/10.1029/2011JF002201>, 2012.
- 20 Powell, R. D.: Glacimarine processes at grounding-line fans and their growth to ice-contact deltas, *Geological Society, London, Special Publications*, 53, 53–73, <https://doi.org/10.1144/GSL.SP.1990.053.01.03>, <https://sp.lyellcollection.org/content/53/1/53>, 1990.
- Powell, R. D. and Alley, R. B.: Grounding-Line Systems: Processes, Glaciological Inferences and the Stratigraphic Record, pp. 169–187, American Geophysical Union (AGU), <https://doi.org/10.1029/AR071p0169>, <https://agupubs.onlinelibrary.wiley.com/doi/abs/10.1029/AR071p0169>, 2013.
- 25 Rignot, E., Mouginot, J., and Scheuchl, B.: Ice Flow of the Antarctic Ice Sheet, *Science*, 333, 1427–1430, <https://doi.org/10.1126/science.1208336>, <https://science.sciencemag.org/content/333/6048/1427>, 2011.
- Scambos, T., Haran, T., Fahnestock, M., Painter, T., and Bohlander, J.: MODIS-based Mosaic of Antarctica (MOA) data sets: Continent-wide surface morphology and snow grain size, *Remote Sensing of Environment*, 111, 242 – 257, <https://doi.org/https://doi.org/10.1016/j.rse.2006.12.020>, <http://www.sciencedirect.com/science/article/pii/S0034425707002854>, remote Sensing of the Cryosphere Special Issue, 2007.
- 30 Scambos, T., Fahnestock, M., Moon, T., Gardner, A., and Klinger., M.: Global Land Ice Velocity Extraction from Landsat 8 (GoLIVE), Version 1. Antarctica., Boulder, Colorado USA. NSIDC: National Snow and Ice Data Center., <https://doi.org/10.7265/N5ZP442B>, 2016.
- Schlegel, R., Diez, A., Löwe, H., Mayer, C., Lambrecht, A., Freitag, J., Miller, H., Hofstede, C., and Eisen, O.: Comparison of elastic moduli from seismic diving-wave and ice-core microstructure analysis in Antarctic polar firn, 60, 220–230, <https://doi.org/DOI:10.1017/aog.2019.10>, <https://doi.org/10.1017/aog.2019.10>, 2019.
- 35 Shreve, R. L.: Movement of Water in Glaciers, *Journal of Glaciology*, 11, 205–214, <https://doi.org/10.3189/S002214300002219X>, 1972.
- Smith, A. M.: Basal conditions on Rutford Ice Stream, West Antarctica, from seismic observations, *J. Geophys. Res.*, 102, 543–552, 1997.
- Smith, W. H. F. and Wessel, P.: Gridding with continuous curvature splines in tension, *Geophysics*, 55, 293–305, 1990.

- Strozzi, T., Luckman, A., Murray, T., Wegmuller, U., and Werner, C. L.: Glacier motion estimation using SAR offset-tracking procedures, *IEEE Transactions on Geoscience and Remote Sensing*, 40, 2384–2391, <https://doi.org/10.1109/TGRS.2002.805079>, 2002.
- Thomas, R. and MacAyeal, D.: Derived Characteristics of the Ross Ice Shelf, Antarctica (Abstract only), *Annals of Glaciology*, 3, 349–349, <https://doi.org/10.3189/S0260305500003220>, 1982.
- 5 Vaughan, D. G., Corr, H. F. J., Bindschadler, R. A., Dutrieux, P., Gudmundsson, G. H., Jenkins, A., Newman, T., Vornberger, P., and Wingham, D. J.: Subglacial melt channels and fracture in the floating part of Pine Island Glacier, Antarctica, *Journal of Geophysical Research: Earth Surface*, 117, <https://doi.org/10.1029/2012JF002360>, <https://agupubs.onlinelibrary.wiley.com/doi/abs/10.1029/2012JF002360>, 2012.
- Walker, R. T., Parizek, B. R., Alley, R. B., Anandakrishnan, S., Riverman, K. L., and Christianson, K.: Ice-shelf tidal flexure and subglacial pressure variations, *Earth and Planetary Science Letters*, 361, 422 – 428, <https://doi.org/https://doi.org/10.1016/j.epsl.2012.11.008>, <http://www.sciencedirect.com/science/article/pii/S0012821X12006164>, 2013.
- 10